Tropical-Forest-Parameter Estimation by Means of Pol-InSAR: The INDREX-II Campaign

Irena Hajnsek, *Member, IEEE*, Florian Kugler, Seung-Kuk Lee, and
Konstantinos Panagiotis Papathanassiou, *Senior Member, IEEE*

Abstract—This paper addresses the potential and limitations of polarimetric synthetic aperture radar (SAR) interferometry (Pol-InSAR) inversion techniques for quantitative forest-parameter estimation in tropical forests by making use of the unique data set acquired in the frame of the second Indonesian Airborne Radar Experiment (INDREX-II) campaign—including Pol-InSAR, light detection and ranging (LIDAR), and ground measurements—over typical Southeast Asia forest formations. The performance of Pol-InSAR inversion is not only assessed primarily at L- and P-band but also at higher frequencies, namely, X-band. Critical performance parameters such as the "visibility of the ground" at L- and P-band as well as temporal decorrelation in short–time repeat-pass interferometry are discussed and quantitatively assessed. Inversion performance is validated against LIDAR and ground measurements over different test sites.

Index Terms—Forest height, polarimetric SAR interferometry (Pol-InSAR), synthetic aperture radar (SAR), temporal decorrelation, tropical forest.

I. INTRODUCTION

TROPICAL RAIN forest ecosystems are highly complex and heterogeneous in terms of species composition and structure and are often difficult to access. Today, radar remote sensing is, for many tropical regions, the only regular available information source. Indeed, Japan Aerospace Exploration Agency's (JAXA) L-band spaceborne synthetic aperture radar (SAR) sensors onboard Japan Earth Resources Satellite-1 (JERS-1) [1] and Advanced Land Observing Satellite (ALOS) [2] demonstrated, in an impressive way, the potential of low-frequency SAR imaging for mapping and monitoring tropical forest ecosystems.

Toward a continuous quantitative forest monitoring, information about horizontal and vertical structures and/or integrative forest parameters such as forest biomass is essential. In contrast to qualitative applications, quantitative approaches by means of SAR are less developed particularly in tropical environments due to the limited data availability and the complexity of such environments. Most of the quantitative approaches are developed on temperate and/or boreal test sites where reference and validation data are easier to collect. The very different structure of tropical forests makes an offhand generalization not possible and requires dedicated experiments for development and validation. Pioneering work based on early airborne SAR experiments addressed tropical forest biomass classification and estimation, hence demonstrating the potential of low-frequency polarimetric SAR (PolSAR) measurements [3], [4]. However, the complexity of radar scattering in forest environments makes the interpretation and inversion of individual SAR and PolSAR observables on the basis of empirical, semiempirical, or theoretical models difficult. The establishment of interferometric SAR (InSAR) techniques for forest monitoring in the late 1990s triggered the first InSAR experiments in the tropics that indicated the potential of interferometric observables at low frequencies for the estimation of vertical structure parameters [5]–[9].

In the last years, the coherent combination of both interferometric and polarimetric observations by means of PolSAR interferometry (Pol-InSAR) was the key for an essential breakthrough in quantitative forest-parameter estimation [10], [11]. Indeed, the quantitative-model-based estimation of forest parameters—based on a single-frequency fully polarimetric single-baseline configuration—has been successfully demonstrated at L- and P-band and, more recently, even at X-band. Several experiments demonstrated the potential of Pol-InSAR techniques to estimate with high accuracy key forest parameters like forest height and above-ground forest biomass over a variety of natural and commercial temperate and boreal test sites characterized by different stand and terrain conditions. Validated results for boreal forests at X- and L-band are shown by [12]. Validated results for temperate forests at X-, L-, and P-band were presented in [11], [13]–[15]. However, the performance in tropical forest conditions could not be validated due to the lack of suitable data.

This lack of actual tropical and subtropical forest Pol-InSAR data sets including both adequate SAR and ground measurements, and the importance of these forest ecosystems with respect to a global forest mapping and monitoring was one of the main drivers for the second Indonesian Airborne Radar Experiment (INDREX-II) that took place in 2004. The analysis, inversion, and validation using this unique data set are presented in this paper. In Section II, the INDREX-II campaign objectives, test sites, and collected data sets are introduced. Section III reviews the physical background and the implementation of Pol-InSAR forest-parameter inversion. In Section IV,

the key issue of the "visibility" of the ground at L- and P-band in dense tropical forest conditions is addressed and evaluated. The accuracy of the obtained forest-height estimates at L- and P-band is assessed against light detection and ranging (LIDAR) and ground measurements in Section V. In addition, a constrained modification of the conventional Pol-InSAR inversion scheme adapted to single channel X-band interferometry is introduced and validated against the LIDAR measurements. In Section VI, short-time temporal decorrelation effects are quantified. Finally, the obtained results are reviewed and discussed in Section VII.

II. INDREX-II CAMPAIGN

A. Campaign Objectives

The main objective of the INDREX-II mission was to build up a unique database of tropical and subtropical test sites with adequate SAR and ground measurements to support the development and validation of bio-/geophysical forest-parameter inversion techniques from multiparameter SAR data. It was expected that the data collected in the frame of the campaign would answer key scientific questions and validate inversion techniques not only at higher (X- and C-bands) but also mainly at lower SAR frequencies (L- and P-band).

Regarding Pol-InSAR inversion techniques, the interest was focused on two main points.

1) The polarimetric diversity of the interferometric coherence and, thus, the information content of the Pol-InSAR observation space depends—in forest environments—on the visibility of the ground under the vegetation layer. This makes the question about the capability of P- or even L-band to penetrate through dense tropical vegetation layer of fundamental importance with respect to the performance of Pol-InSAR techniques in tropical forest environments.
2) The demonstration and quantitative evaluation of the Pol-InSAR inversion performance in different tropical and subtropical forest conditions.

Both points will be addressed, discussed, and analyzed in the following sections.

B. Test Sites and Ground Measurements

Two main test areas both located on the island of Borneo, Kalimantan, Indonesia, have been selected for INDREX-II. The first test site is the Mawas conservation area (latitude: $-2.15°$, longitude: $114.45°$) located in Central Kalimantan in the vicinity of its capital city Palangkaraya. The second area is located in East Kalimantan in the vicinity of the city of Balikpapan (latitude: $-1.10°$, longitude: $116.82°$). The two areas comprise the main broad forest types in Indonesia: lowland dipterocarp, peat swamp, and mangrove forest, as well as a variety of the common plantation types such as oil palm and rubber tree. Eight test sites have been defined, two located in the Mawas area and six in the Balikpapan area. Our investigations concentrate on two of the eight test sites that represent typical forest formations of Southeast Asia like lowland dipterocarp

and peat-swamp forests with disturbed and undisturbed stands at very different terrain conditions.

1) The *Sungai Wain* test site is a hilly area with steep slopes located close to the city of Balikpapan in East Kalimantan. It is covered by typical lowland dipterocarp forests with biomass levels up to 400 t/ha and tree heights up to 60 m. On a large scale, this forest type can be seen as rather homogeneous, while on a small scale, patches of different succession stages go along with changes in height. Large areas were burnt during the El Niño events of 1982 and 1998. They are now covered with Macaranga, a secondary forest type.

A 15.4-ha large forest plot was established in the Sungai Wain dipterocarp forest, with a 540-m length and 286-m width. Within this plot, 26 blocks of 26×32 m (in total, 2.1 ha) have been registered. The catalogue includes diameter at breast height (DbH) and tree height measurements for each canopy tree with DbH $\geq$ 10 cm.

2) The *Mawas* test site is located in central Kalimantan. It is, in general, flat including several large (ombrogenous) peat domes and is covered by tropical peat-swamp forest types. Forest height varies gradually from relatively tall (30 m) and dense forests at the edges toward small (15 m or lower) and open forests at the center of a dome with biomass levels from 20 to 350 t/ha. Mixed swamp (some topogenous) and floodplain forests are located along the river flow. The southern and eastern parts are disturbed by excessive drainage (through canals) and peat forest fires.

In August 2007, LIDAR measurements were performed with a swath width of about 300 m along a 22-km-long strip located in the middle of the SAR swath. The spatial resolution is of 3–4 m, dependent on the amount of returning samples; the pixel density decreases from the center (nadir) to the corners of the image. From the LIDAR raw data, forest-height and ground terrain digital elevation models (DEM) have been processed [16], [17]. During the three years between the LIDAR and the radar campaign, changes in the forest caused by tree growth (on the order of 1–2 m), tree dieback, and human impact may be an additional error source when comparing LIDAR and radar measurements to each other.

C. SAR Data

The SAR data acquisitions have been performed with the German Aerospace Center (DLR)'s experimental airborne SAR system (E-SAR) in November and December 2004. For each test site, the following modes have been acquired:

1) one X-band single-pass InSAR acquisition at a single channel (VV polarization) for DEM generation;
2) two C-band dual-polarization acquisitions (one in the VH–HH and the other in the HV–VV mode);
3) three L-band quad-polarization acquisitions flown in a repeat-pass InSAR mode;
4) four P-band quad-polarization acquisitions flown in a repeat-pass InSAR mode.

The spatial (repeat-pass) baselines at L- and P-bands have been chosen to cover the same height sensitivity and to allow an

TABLE I
INDREX-II DATA SETS

Test Site	Frequency	Baseline [m] / kz range	Acquisition InSAR/PolSAR
Sungai Wain	L-band	10 / 0.04 – 0.21	Repeat / Quad
Sungai Wain	P-band	30 / 0.04 – 0.17	Repeat / Quad
Mawas River	X-band	0.8 / 0.07 – 0.13	Single / VV
Mawas River	L-band	05 / 0.03 – 0.16	Repeat / Quad
Mawas River	L-band	10 / 0.08 – 0.34	Repeat / Quad
Mawas River	L-band	15 / 0.11 – 0.51	Repeat / Quad
Mawas River	P-band	15 / 0.03 – 0.13	Repeat / Quad
Mawas River	P-band	30 / 0.06 – 0.26	Repeat / Quad
Mawas River	P-band	30 / 0.07 – 0-27	Repeat / Quad
Mawas River	P-band	40 / 0.08 – 0.40	Repeat / Quad
Mawas Dome	X-band	0.8 / 0.07 – 0.13	Single / VV
Mawas Dome	L-band	05 / 0.04 – 0.17	Repeat / Quad
Mawas Dome	L-band	05 / 0.02 – 0.15	Repeat / Quad
Mawas Dome	P-band	15 / 0.03 – 0.13	Repeat / Quad

optimum inversion performance with respect to the expected forest conditions.

As INDREX-II was performed at the beginning of the rainy season, some of the data acquisition flights had to be flown under windy conditions. Consequently, some of the repeat-pass acquisitions (i.e., at L- or P-band) particularly in the Mawas Dome test site have been affected by wind-induced temporal decorrelation. For this reason, the acquisitions have been repeated, providing the possibility to analyze temporal decorrelation effects. Table I provides a summary of the SAR data sets used in this work. Note that the Mawas Dome data sets are strongly affected by temporal decorrelation.

III. Pol-InSAR PARAMETER INVERSION

The key observable used in Pol-InSAR applications is the complex interferometric coherence $\tilde{\gamma}$ (including both the interferometric correlation coefficient and interferometric phase) measured/estimated at different polarizations (indicated by the unitary vector $\vec{w}$ [10], [11]). $\tilde{\gamma}$ is given by the normalized cross correlation of the two SAR images obtained from the interferometric acquisition s_1 and s_2

$$\tilde{\gamma}(\vec{w}) := \frac{\langle s_1(\vec{w}) s_2^*(\vec{w}) \rangle}{\sqrt{\langle s_1(\vec{w}) s_1^*(\vec{w}) \rangle \langle s_2(\vec{w}) s_2^*(\vec{w}) \rangle}}. \quad (1)$$

The coherence depends on instrument and acquisition parameters as well as on dielectric and structural parameters of the scatterer. A detailed discussion of system-induced coherence errors can be found in [18]. After the calibration of system-induced decorrelation contributions and compensation of spectral decorrelation in azimuth and range, the estimated interferometric coherence can be decomposed into three main decorrelation processes [19]

$$\tilde{\gamma} := \tilde{\gamma}_{\text{Temp}} \quad \gamma_{\text{SNR}} \quad \tilde{\gamma}_{\text{Vol}}. \quad (2)$$

1) Temporal decorrelation $\tilde{\gamma}_{\text{Temp}}$ can be real (i.e., effecting the absolute value of $\tilde{\gamma}$ only) or complex (i.e., biasing the phase of $\tilde{\gamma}$). It depends on the structure and the temporal stability of the scatterer, the temporal baseline of the interferometric acquisition, and the dynamic environmental processes occurring in the time between the acquisitions.

2) Noise decorrelation γ_{SNR} is introduced by the additive white noise contribution on the received signal [20], [21]. It affects primarily the scatterers with low (back-)scattering and is, in general, of secondary importance when looking at a forest at conventional frequencies.

3) Volume decorrelation $\tilde{\gamma}_{\text{Vol}}$ is the decorrelation caused by the different projection of the vertical component of the scatterer into the two images $s_1(\vec{w})$ and $s_2(\vec{w})$. $\tilde{\gamma}_{\text{Vol}}$ is directly linked to the vertical distribution of scatterers $F(z)$ through a (normalized) Fourier transformation relationship

$$\tilde{\gamma}_{\text{Vol}} = \exp(i\kappa_z z_0) \frac{\int_0^{h_V} F(z') \exp(i\kappa_z z') dz'}{\int_0^{h_V} F(z') dz'} \quad (3)$$

where h_V is the height of the volume and κ_z is the effective vertical (interferometric) wavenumber that depends on the imaging geometry and the radar wavelength λ

$$\kappa_z = \frac{\kappa \Delta\theta}{\sin(\theta_0)} \qquad \kappa = n\frac{2\pi}{\lambda} \quad (4)$$

and $\Delta\theta$ is the incidence angle difference between the two interferometric images induced by the baseline. z_0 is a reference height, and $\varphi_0 = \kappa_z z_0$ is the corresponding interferometric phase. For monostatic acquisitions, as flown in INDREX-II, $n := 2$, while for bistatic acquisitions, $n := 1$. Accordingly, $\tilde{\gamma}_{\text{Vol}}$ contains the information about the vertical structure of the scatterer and is therefore the key observable for quantitative forest-parameter estimation [10], [11].

The estimation of vertical forest structure parameters from interferometric measurements can be addressed as a two-step process: In the first step (modeling), $F(z)$ is parameterized in terms of a limited set of physical forest parameters that are related through (3) to the interferometric coherence. In the second step (*inversion*), the volume contribution of the measured interferometric coherence is then used to estimate $F(z)$ and to derive the corresponding parameters. A widely and successfully used model for $F(z)$ is the so-called random volume over ground (RVoG), a two-layer model consisting of a volume and a ground layer [22], which can be described as

$$F(z) = \tilde{m}_V \, e^{\left(\frac{2\sigma}{\cos(\theta_0)} z\right)} + m_G \, e^{\left(\frac{2\sigma}{\cos(\theta_0)} h_V\right)} \delta(z - z_0) \quad (5)$$

where m_V and m_G are the ground and volume scattering amplitudes and σ is a mean extinction coefficient. Equation (5) leads to

$$\tilde{\gamma}_{\text{Vol}} = \exp(i\kappa_z z_0) \frac{\tilde{\gamma}_{V0} + m}{1 + m}. \quad (6)$$

The phase $\varphi_0 = \kappa_z z_0$ is related to the ground topography z_0, and m is the effective ground-to-volume amplitude ratio accounting for the attenuation through the volume

$m = m_G/(m_V I_0)$. $\tilde{\gamma}_{V0}$ is the volume decorrelation caused by the vegetation layer only, given by

$$\tilde{\gamma}_{V0} = \exp(i\kappa_z z_0) \frac{\int_0^{h_V} \exp(i\kappa_z z') \exp\left(\frac{2\sigma z'}{\cos\theta_0}\right) dz'}{\int_0^{h_V} \exp\left(\frac{2\sigma z'}{\cos\theta_0}\right) dz'}. \quad (7)$$

Neglecting temporal decorrelation and assuming a sufficient calibration/compensation of system- (e.g., SNR) and geometry- (range/azimuth spectral shift) induced decorrelation contributions, (6) can be inverted in terms of a quad-polarization single-baseline acquisition [11], [13], [23], [24]. Assuming no response from the ground in one polarization channel (i.e., $m_3 = 0$), the inversion problem has a unique solution and is balanced with five real unknowns ($h_V, \sigma, m_{1-2}, \varphi_0$) and three measured complex coherences $[\tilde{\gamma}(\vec{w}_1) \quad \tilde{\gamma}(\vec{w}_2) \quad \tilde{\gamma}(\vec{w}_3)]$ each for any independent polarization channel [23]

$$\min_{h_V, \sigma, m_i, \phi_0} \left\| \begin{bmatrix} \rho & \rho & \rho \\ \tilde{\gamma}(w_1) & \tilde{\gamma}(w_2) & \tilde{\gamma}(w_3) \end{bmatrix}^{\mathrm{T}} \right.$$

$$\left. - \begin{bmatrix} \tilde{\gamma}_{\mathrm{Vol}}(h_V, \sigma, m_1) & \tilde{\gamma}_{\mathrm{Vol}}(h_V, \sigma, m_2) & \tilde{\gamma}_{V0} \exp(i\phi_0) \end{bmatrix}^{\mathrm{T}} \right\|. \quad (8)$$

Equation (8) is used to invert INDREX-II data sets at L- and P-band. The same regularization ($m_3 = 0$) has been used at L-band as well as at P-band. Because of the dense vegetation layer, a modified regularization at P-band is not required. Note that the assumption for no ground response is not necessarily linked to the HV channel.

IV. EFFECT OF THE GROUND

Starting with the first scientific question expected to be answered from INDREX-II, the visibility of the ground is investigated. The investigation is focused on the densest vegetated test site, the Sungai Wain test site covered by dense lowland dipterocarp forests with individual tree heights up to 60 m and a mean biomass level up to 400 t/ha. A secondary low-vegetation layer located on the ground additionally increases the attenuation of any ground-scattering component. However, the hilly terrain of the site can be used to evaluate the terrain dependence of the individual parameters and conclude on the visibility of the ground.

The strong polarized behavior of ground scattering (including direct ground and/or dihedral scattering) combined with the directivity of the dihedral scattering component make the type and amount of ground scattering strongly dependent on the terrain slope in range direction. This supports the idea of "seeing" the ground through the modulation of the polarimetric signature by the terrain slope in the Sungai Wain data set.

Fig. 1 shows the 2-D histogram of the polarimetric alpha angle [25] that characterizes the nature of the polarimetric scattering process as a function of the terrain range slope at L- (top) and P-band (bottom). Positive slopes indicate an inclination toward the radar, while negative slopes indicate inclinations away from the radar. In both cases, the alpha angles are around
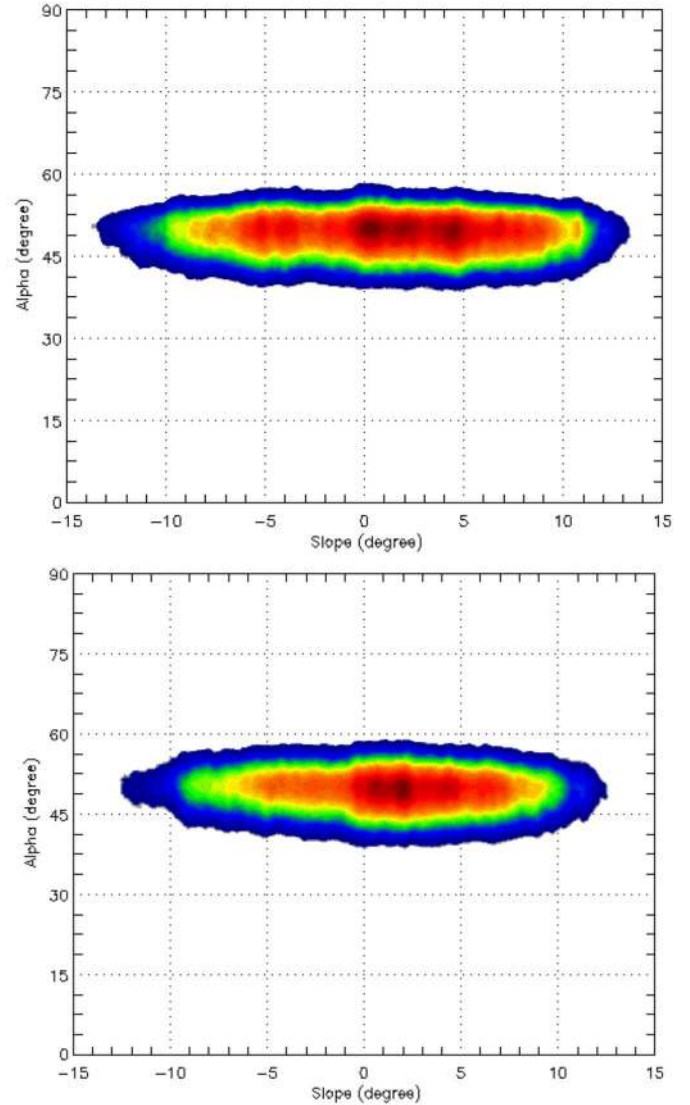

Fig. 1. Polarimetric alpha-angle histogram as a function of range terrain slopes at (top) L- and (bottom) P-band.

$50°$ that, combined with the high polarimetric entropy levels obtained, indicates a dominant volume scattering component. The absence of any slope dependence at L-band as well as at P-band can be seen as an indicator for the absence of a ground-scattering component signature.

A far more sensitive indicator for the visibility of the ground is the location of the scattering phase center estimated in the interferogram. According to (6), the location of the interferometric phase center within the vegetation layer depends on the ground-scattering amplitude. Larger ground-to-volume amplitude ratio m values correspond to stronger ground-scattering amplitudes and move the phase center toward the ground and *vice versa*. The polarization dependence of m relates the variance of the interferometric phase center as a function of polarization directly to the variance of the amplitude of the ground-scattering component. In order to illustrate this, Fig. 2 shows the coherence region of the interferometric coherence [28]–[30] as a gray cloud of coherence loci plotted on the unit circle for a stand within the Sungai Wain site at L- (top) and P-band (bottom). The coherence region is defined as the
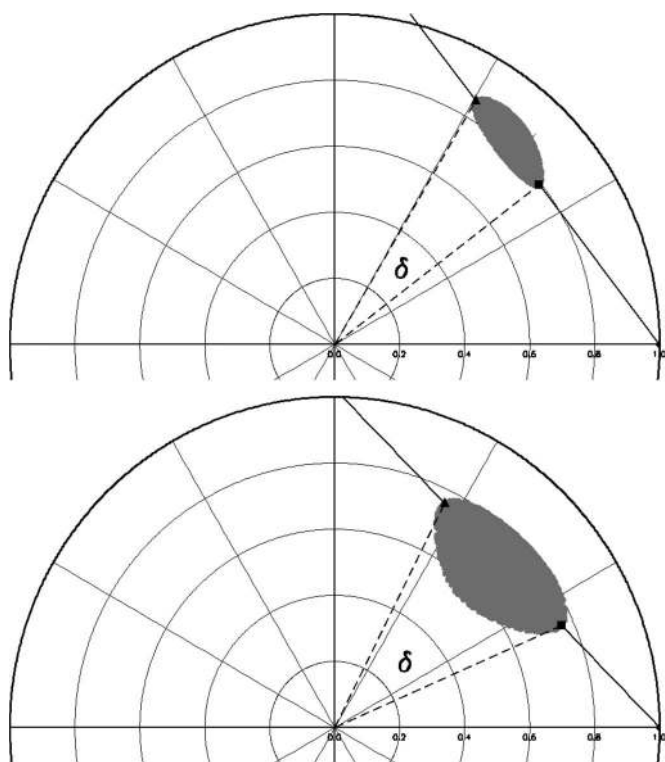
Fig. 2. Coherence region at (top) L- and (bottom) P-band for the same forest stand (Sungai Wein test site).

region that includes the loci of the (complex) interferometric coherences obtained for all polarizations [31]. Consequently, the angle δ that corresponds to the maximum variation of the phase center with polarization is a sensitive indicator for the amount of ground scattering visible. In the case of an increased attenuation of the ground-scattering component, the coherence region shrinks and becomes a point in the limit. In this case, $\delta = 0$. Of course, one has to account for the variance of the amplitude and, primarily, the phase of $\tilde{\gamma}(\vec{w}_i)$ induced by the nonunity coherence using a sufficient large number of looks when estimating $\tilde{\gamma}(\vec{w}_i)$. In the case of Fig. 2, 81 independent looks have been used. In order to make a direct comparison possible, the stand is located on flat terrain and has a similar wavenumber at both frequencies. The variation of the interferometric phase at L-band in Fig. 2 shows the visibility of a polarized ground-scattering component under the vegetation layer. The phase difference is on the order of $22°$ corresponding to 9.5 m. At P-band, the height difference between the phase centers is larger, about $43°$ corresponding to 13.5 m, indicating a stronger ground-scattering component at P-band than at L-band. Note that a polarization-dependent propagation through the volume layer caused by orientation effects in the vegetation structure and expressed by a polarization-dependent extinction coefficient in (7) can also introduce a variance of the phase center with polarization. However, this is rather unusual for dense forest vegetation at L-band but also at P-band.

Fig. 3 shows the 2-D histogram of the δ angle (scaled by using the vertical wavenumber in meters) as a function of terrain range slope obtained at L- (top) and P-band (bottom). The height difference decreases monotonically at both frequencies as the range slope decreases, indicating the expected stronger
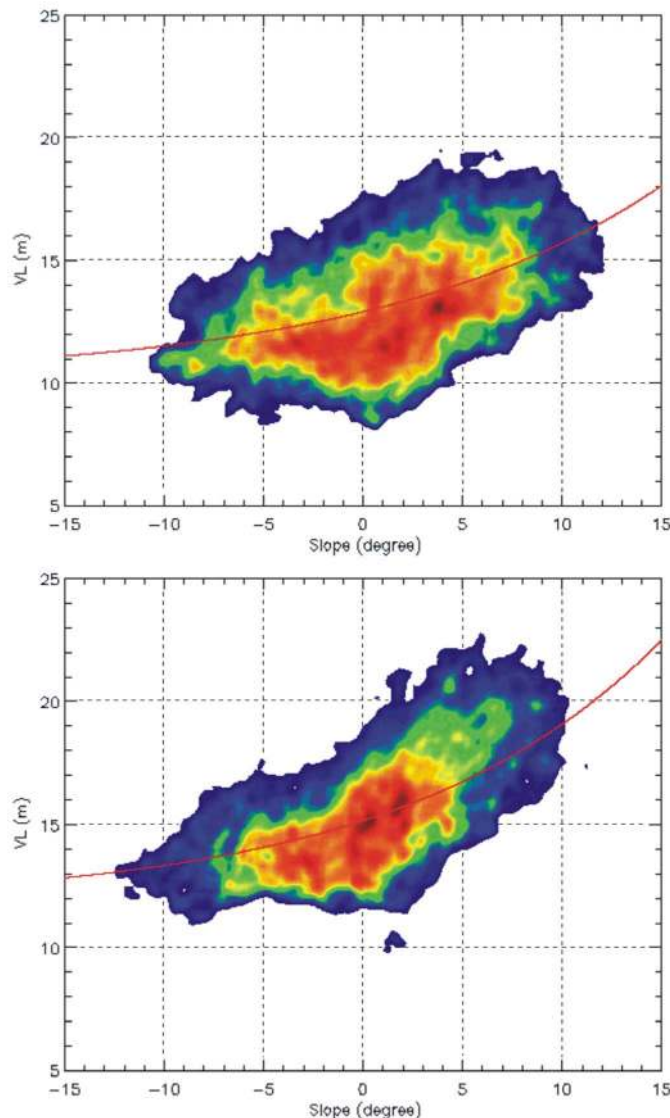

Fig. 3. Phase center height difference (maximum) histogram as a function of range terrain slopes at (top) L- and (bottom) P-band.

ground response at higher (i.e., positive) slopes and, thus, the visibility of the ground at L- and P-bands across the whole site. Positive slopes are tilted toward the radar while negative slopes are tilted away from the radar. The height difference is, as expected, larger at P-band than at L-band through the whole range of slopes, indicating the visibility of a stronger ground component in P-band compared to L-band. Because there is no reason that orientation effects in vegetation are correlated to terrain slope, Fig. 3 is a direct proof for the visibility of the ground at both frequencies in dense tropical forest environments.

V. INVERSION RESULTS

Forest height was estimated and validated against the ground measurements for both test sites: the Mawas peat-swamp forest (i.e., Mawas River test site) and the Sungai Wain lowland dipterocarp forest. As the reference height for validation, the so-called "H100" from forest measurements [32] was used, which
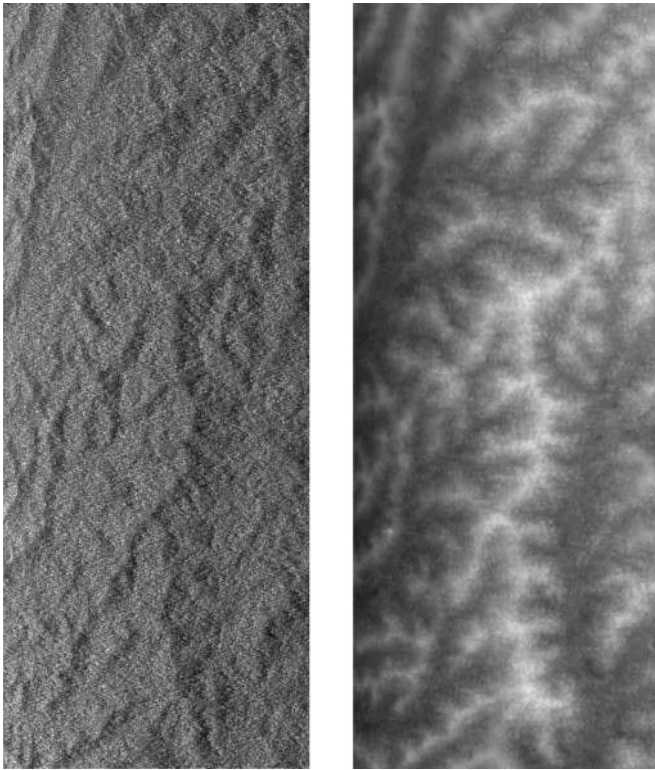
Fig. 4. Sungai Wain test site. (Left) L-band HH amplitude image (grayscale) near range left side. (Right) DEM calculated from X-band data (black = 50 m, white = 180 m AMSL) 3.5 × 6.5 km.

is defined as the mean height of the 100 highest trees per hectare [33]. H100 is a forestry standard canopy top height measure and corresponds quite well to radar forest-height estimates, as it is calculated out of the trees forming the canopy, i.e., the height of the volume.

For the Sungai Wain test site, the ground measurements where converted to H100 values for each block individually. In the Mawas test site, the H100 has been obtained from the LIDAR data by taking the maximum value of a 10 × 10 m window (corresponding to 1/100 of a hectare) [33], [34].

A. Sungai Wain Test Site

Fig. 4, on the left, shows an L-band HH amplitude image of the Sungai Wain scene while, on the right, the X-band DEM is shown. The scene is completely covered with forest situated in hilly terrain with steep slopes (up to 30°). Variations in the amplitude are only due to changes in topography. For accurate inversion, the estimation of incidence angle and interferometric baseline needs to account for the topographic variation. In addition, terrain adaptive range spectral filtering using the low-pass filtered X-band InSAR DEM has been applied, on the price of a variable spatial range resolution across the image.

The measured forest heights (H100) are ranging from 20 up to 40 m, whereas most of the plots have heights between 24 and 28 m as shown by the blue histogram in Figs. 5 and 6.

The normalized histograms of the heights obtained at L- and P-bands over the whole plot of 200 × 500 m are shown in red in Figs. 5 and 6, respectively. The L-band height estimates range
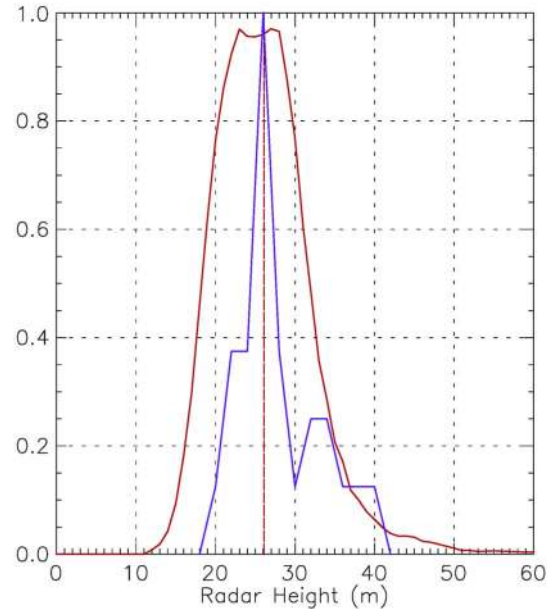

Fig. 5. Forest-height histograms. (Blue) Ground measured heights. (Red) Pol-InSAR height estimates at L-band (Sungai Wain test site).
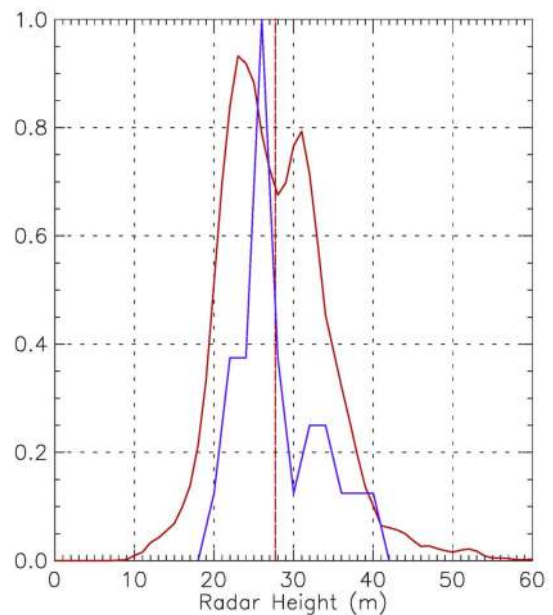

Fig. 6. Forest-height histograms. (Blue) Ground measured heights. (Red) Pol-InSAR height estimates at P-band (Sungai Wain test site).

from 15 to 45 m with a mean forest height of about 28 m. At P-band, the obtained results range from 13 to 43 m with a similar mean of about 26 m. Overestimation (i.e., estimated heights above 45 m) appears as a consequence of temporal or other uncompensated decorrelation contributions. This can be due to remaining SNR and processing decorrelation contributions. In particular, accurate image coregistration becomes challenging in sloped terrain and low coherence levels. At both frequencies, the radar estimates cover the same range of heights and have a similar height distribution and a mean value better than 10% of the mean given by the ground measurements (i.e., 27 m, see blue histogram in Figs. 5 and 6). The maxima and minima diverge on the order of 5 m, probably due to an
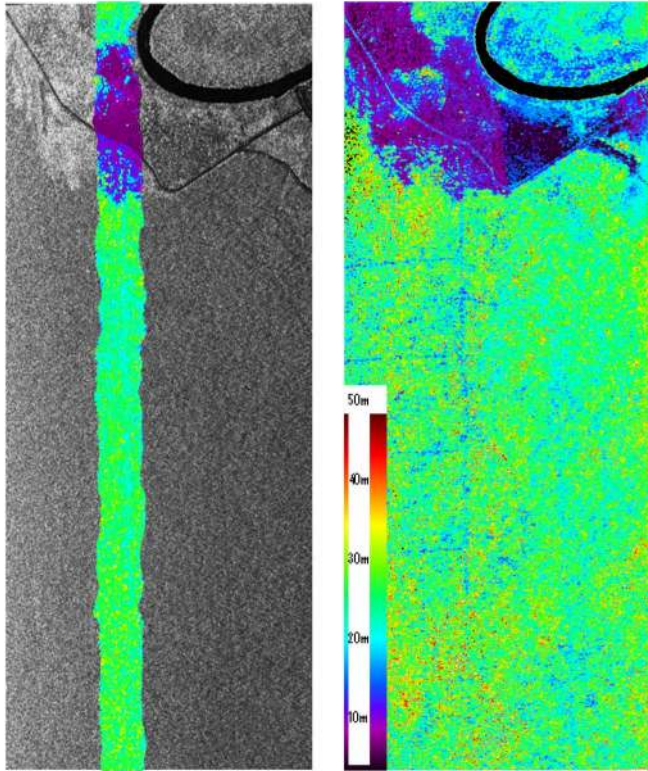
Fig. 7. Mawas River test site. (Left) (grayscale; near range: Left) P-band amplitude image with (color) LIDAR H100 measurements. (Right) P-band forest-height map, combination of four baselines, scaled from 0 to 50 m (region larger than 50 m are white). 3.5 × 6.5 km.

insufficient number of ground measurement samples. It appears that P-band is able to resolve the bimodal height distribution (see Fig. 6) as measured on the ground while L-band is able to resolve only the envelope distribution (see Fig. 5). As the spatial resolution and the vertical wavenumber are almost the same for both frequencies, and furthermore, the interferometric coherence levels are comparable, the reason can be a higher sensitivity of L-band to temporal decorrelation effects that lead to a reduced estimation accuracy.

B. Mawas River Test Site

The amplitude image of the P-band HH channel for the Mawas River test site is shown in Fig. 7 (left). The amplitude image already indicates the terrain flatness. The transition from the burned area located on the top of the image to the forested area covering 2/3 of the image is characterized partly by low (up to 2 m) secondary shrublike vegetation and, particularly at the edge of the forest, by patches of heavily disturbed forest. The river crosses the upper part of the image embedded in a secondary riverine forest. The LIDAR strip is superimposed on the amplitude image. Forest height along the LIDAR strip is constant within ±5 m around 27 m with lower heights in the parts close to the river and the disturbed forest areas. The terrain rises from the middle to the right part of the image toward the peat dome (covered by the relevant forest part) from 20 to 25 m above mean sea level (AMSL) in height while the area around the river has a constant height of 17.5 m AMSL.
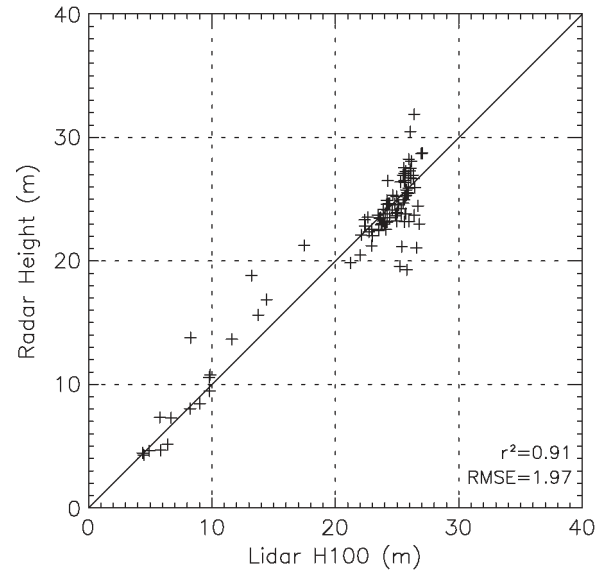

Fig. 8. Pol-InSAR height estimates at L-band versus LIDAR H100 validation plot for the Mawas River test site (100 samples).

Forest heights were estimated at L- and P-bands using a multiple-baseline inversion approach. The reason for this is in the E-SAR acquisition geometry at L- and P-bands where the radar look angle changes from near to far range from 25° to 55° [35]. This variation of the look angle goes along with a change of baseline (up to a factor of four), implying an inversion performance that varies along range. An optimum inversion performance across the whole range can then be achieved by combining the optimum range of multiple baselines. Accordingly, regions with low inversion performance caused by too high or too low volume sensitivity characterized by a vertical wavenumber larger than 0.20 or smaller than 0.05 are masked out for each individual baseline. Also, areas with a coherence lower than 0.3 are masked. The valid areas of each baseline are then combined together toward a single height image. In the case of two valid height estimates, a weighted height is used, reducing, in these areas, errors caused by nonsystematic uncompensated decorrelation contributions [23], [24].

Results were validated against the H100 derived from the LIDAR data. For this, the LIDAR H100 strip was divided into 100 subplots, and for each plot, the mean H100 is validated against the corresponding mean forest height as obtained from the Pol-InSAR inversion.

An L-band Pol-InSAR height map was obtained by combining height estimates from three baselines (5, 10, and 15 m). The comparison against the LIDAR H100 is shown in Fig. 8: with an r^2 of 0.91 and an RMSE of 1.97 m, for a height range from 5 to 28 m, indicating an estimation accuracy better than 10% which lies within the estimation accuracy of the LIDAR H100 set.

The P-band Pol-InSAR height map has been obtained by combining height estimates from four baselines (15, 30, 30, and 40 m) and is shown on the right of Fig. 7. The black dots in the near range are masked according to the wavenumber and coherence criteria discussed previously. In the forested part, the logging trails caused by logging activities 10–15 years ago appear clearly. For validation, two independent 30-m baselines formed by four different tracks (first baseline using track 1402
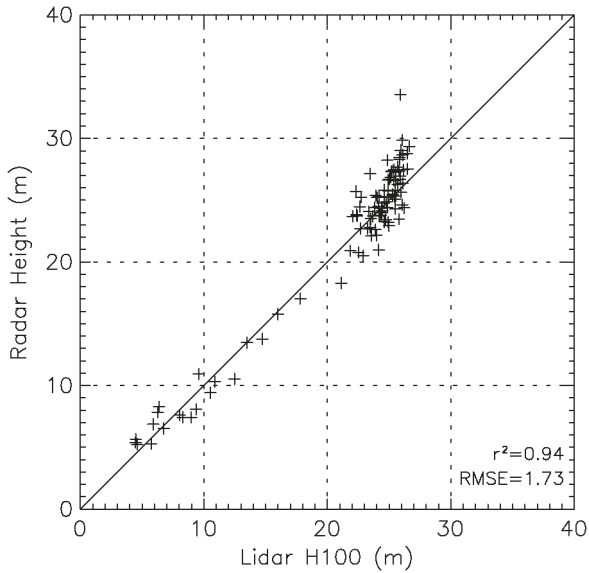
Fig. 9. Pol-InSAR height estimates at P-band versus LIDAR H100 validation plot for the Mawas River test site (100 samples, tracks 1402 and 1408).
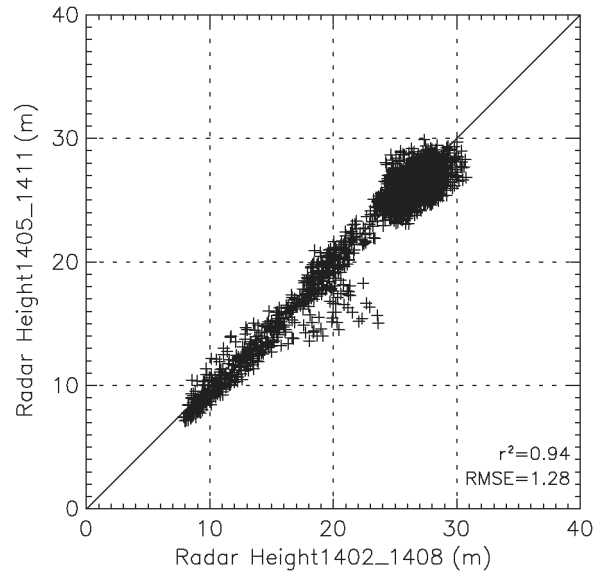

Fig. 11. Pol-InSAR height estimates at P-band (tracks 1405 and 1411) versus Pol-InSAR height estimates at P-band (tracks 1402 and 1408) for the Mawas River test site (3000 samples).
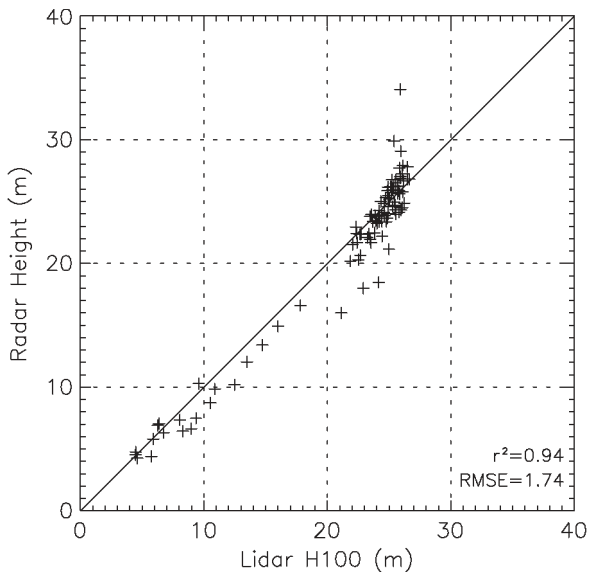

Fig. 10. Pol-InSAR height estimates at P-band versus LIDAR H100 validation plot for the Mawas River test site (100 samples, tracks 1405 and 1411).
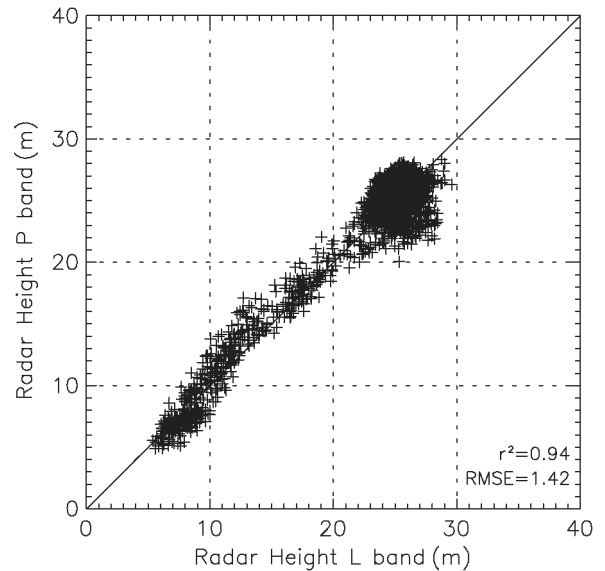

Fig. 12. Pol-InSAR height estimates at P-band (all tracks) versus Pol-InSAR height estimates at L-band (all scenes) for the Mawas River test site (3000 samples).

and 1408, second baseline using track 1405 and 1411) were used. In this case, a single baseline is sufficient as the optimum performance region for both baselines covers the whole LIDAR strip. Figs. 9 and 10 show the corresponding validation plots: The correlation coefficient with an r^2 of 0.94 for both baselines is quite high, and the RMSE is 1.73 m for the first and 1.74 m for the second baseline clearly below 2 m, hence showing an estimation accuracy better than 10% of the mean forest height. Clearly, the estimation performance is within the LIDAR estimation performance used as reference. Individual single points located particularly in the higher forest region tend to be overestimated probably due to uncompensated decorrelation effects. The comparison of the heights obtained from the two 30-m baselines is shown in Fig. 11 and is characterized by an r^2 of 0.94 and an RMSE of 1.28 m for a height range from 5 to 28 m,

indicating the high consistency in the obtained results. The differences may be caused by the different amount of temporal decorrelation in the individual interferograms. The comparison was performed over 3000 samples distributed over the whole optimum performance region.

Compared to P-band, the L-band estimates (see Fig. 8) appear slightly noisier. This is because L-band is more affected by temporal decorrelation (see Section VI). The comparison of the L-band against the P-band estimates shown in Fig. 12 is based on the forest-height maps obtained by combining all available baselines (i.e., the 15-, 30-, 30-, and 40-m baselines at P-band and the 5-, 10-, and 15-m baselines at L-band) in order to obtain a performance comparison over 3000 samples distributed over the whole image: The obtained r^2 of 0.94 and
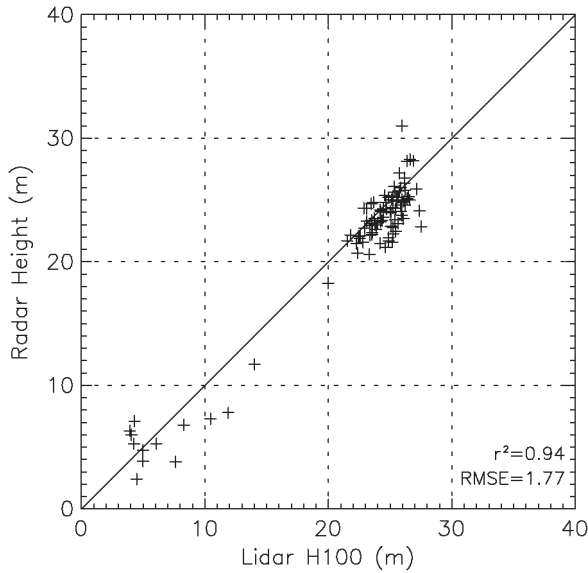
Fig. 13. InSAR height estimates (9) at X-band versus LIDAR H100 validation plot for the Mawas River test site (100 samples).

Fig. 14. InSAR phase center height at X-band versus LIDAR H100 validation plot for the Mawas River test site (100 samples).

an RMSE of 1.42 m manifest the consistency of the obtained estimates, indicating the validity of the physical structure underlying the Pol-InSAR inversion process. Divergences on the order of 2–3 m can be due to the variance introduced by temporal decorrelation and/or geolocation inaccuracy when transforming the P-band results to the L-band geometry.

In contrast to L- and P-band, X-band interferometry was performed in a single-pass mode. Consequently, the X-band interferometric coherence estimates are unaffected by temporal decorrelation. However, the availability of a single X-band channel (VV polarization) only makes the inversion of (6) by means of (8) not possible. A solution can be enforced by simplifying $F(z)$ and/or making use of *a priori* information. At higher frequencies, the vegetation extinction increases, attenuating more and more the strongly polarized ground-scattering contribution. One obvious approximation toward a simplified single-channel inversion scenario is to discard the ground-scattering component [assuming that $m = 0$ in (6)]. In this case, the single-channel interferometric inversion problem has three unknowns (i.e., height, extinction, and topographic phase) and only one (complex) observable. Using the ground phase obtained from the LIDAR ground DEM, it is then possible to obtain a balanced inversion problem

$$\min_{h_V, \sigma_0} \| \tilde{\gamma}(\vec{w}) - \tilde{\gamma}_V(h_V, \sigma | \phi_0 = \phi_{\text{DEM}}) \|. \quad (9)$$

Equation (9) can be inverted by a single interferometric channel providing forest-height estimates.

Similar to the L- and P-band validation, the LIDAR H100 strip was divided into 100 subplots. For each of the subplots, the mean H100 is used to validate the corresponding mean forest height as obtained from the X-band inversion. The validation plot is shown in Fig. 13. An r^2 of 0.94 and an RMSE of 1.77 m for a height range of 5–29 m prove a surprisingly good estimation performance at X-band. The estimated extinction values range from 0.1 up to 0.9 dB/m with a mean value on the order of 0.3 dB/m.
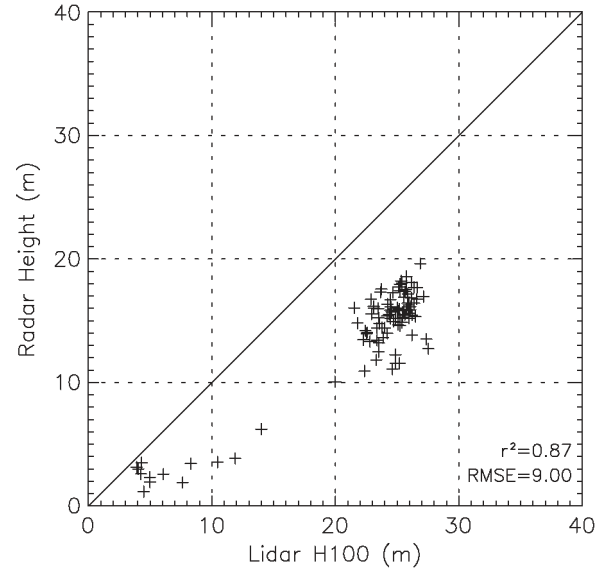
One has to keep in mind that (6) assumes a homogeneous vegetation layer. Volume inhomogeneities that introduce an additional variation of the phase center, for example, in the case of sparse forests with high single tree extinction (i.e., at higher frequencies), can bias the estimated volume coherence by an additional decorrelation term that corresponds to the "forest topography" variation within the estimation window. However, the fact that the obtained inversion results are not biased indicates that, at least for the Mawas case, the introduced bias is of secondary importance.

In Fig. 14, the height of the scattering center at X-band is plotted against the LIDAR H100 height: The comparison of the estimated phase centers with the ground makes it obvious that the scattering center of X-band is located clearly below the forest canopy. The RMSE of 9 m corresponds to the mean penetration depth into vegetation at X-band, indicating a higher estimation variance compared to forest top height (H100).

The r^2 of 0.87 is lower than the corresponding r^2 of 0.94 obtained from the height estimates of (9). This is a significant result indicating the systematic error that underlies height-estimation approaches based on the assumption that the X-band phase center is located on the top of the canopy [5], [26], [27]. On the other hand, it indicates the potential of Pol-InSAR inversion schemes.

In the absence of an external ground DEM, an alternative way to enforce a balanced inversion problem is to fix the extinction value. Ignoring the ground phase, by considering the absolute values only, a single parameter inversion problem is obtained

$$\min_{h_V} \| \, |\tilde{\gamma}(\vec{w})| - |\tilde{\gamma}_V(h_V, \phi_0 | \sigma = \sigma_0)| \, \|. \quad (10)$$

Inversion has been performed using different extinction values; the best performance has been obtained for extinction around 0.3 dB/m that corresponds to the mean extinction value obtained from (9). Fig. 15 shows the validation plot for the forest-height estimates obtained by applying (10) and assuming an
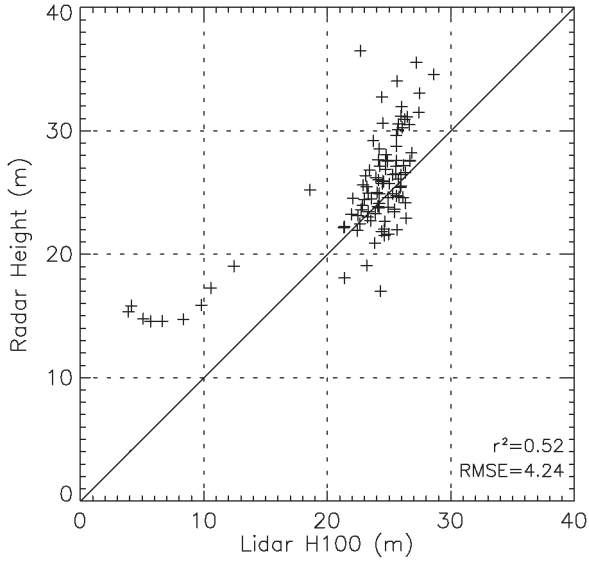
Fig. 15. InSAR height estimates (10) at X-band versus LIDAR H100 validation plot for the Mawas River test site (100 samples).

extinction of 0.3 dB/m. The r^2 of 0.52 and an RMSE of 4.24 m indicate a clearly inferior performance when compared to the inversion results obtained by means of (9). This is a direct consequence of the strong variation of the extinction value across the forest: An underestimation of the real extinction leads to overestimated forest heights and vice versa. Looking at Fig. 15, one sees that, particularly in the middle and lower forest parts, the height is overestimated due to the underestimation of extinction. Finally, under the assumption that both ground topography or extinction level are known, a height inversion independent of the ground-to-volume ratio becomes theoretically possible. However, also in this case, the variation of the extinction value across the forest will limit the performance.

VI. TEMPORAL DECORRELATION

The quantification of temporal decorrelation in repeat-pass interferograms is discussed next based on the data sets acquired over the Mawas Dome test site that, in contrast to the Mawas River data sets discussed in the previous section, are significantly affected by temporal decorrelation. The most common temporal decorrelation effect over a forested terrain is the wind-induced movement of scatterers within the canopy layer, for example, leaves, branches, etc. In terms of the RVoG model, this corresponds to a change in the position of the scattering particles within the volume. However, in this case, the scattering amplitudes as well as the propagation properties of the volume remain the same. Assuming further that the scattering properties of the ground do not change, the RVoG model with temporal decorrelation in the volume component becomes [23], [36]

$$\tilde{\gamma}_{\mathrm{Vol}}(\vec{w}) = \exp(i\kappa_z z_0) \frac{\gamma_{\mathrm{Temp}}\tilde{\gamma}_{V0} + m(\vec{w})}{1 + m(\vec{w})} \qquad (11)$$

where γ_{Temp} denotes the correlation coefficient describing the temporal decorrelation of the volume scatterer. Inversion of for-

est height by means of (11) without accounting or compensating for γ_{Temp} leads to overestimated results [10]. In the special case of a zero spatial baseline interferogram (i.e., $\kappa_z = 0$ and $\tilde{\gamma}_{V0} = 1$), γ_{Temp} and $\tilde{\gamma}_{V0}$ can be separated from each other

$$\tilde{\gamma}_{\mathrm{Vol}}(\vec{w}) = \frac{\gamma_{\mathrm{Temp}} + m(\vec{w})}{1 + m(\vec{w})}. \qquad (12)$$

However, in a general case of nonzero spatial baselines, the two contributions are superimposed and cannot be separated from each other on a single-baseline basis and/or without *a priori* information.

One way to obtain sensible estimates for γ_{Temp} at L- or P-band is to make use of the forest heights obtained by the X-band inversion h_V^X as derived by means of (10). The X-band forest-height estimates can be used to approximate the volume decorrelation contributions $|\tilde{\gamma}_{\mathrm{Vol}}^L(HV)|$ at L- or P-band. However, this is not offhand possible and requires additional assumptions. Constraining the analysis to the HV channels, one can assume zero ground scattering $(m(HV) = 0)$. Assuming further a zero extinction (i.e., $\sigma_L = 0$), (7) becomes

$$\left|\tilde{\gamma}_{\mathrm{Vol}}^L(HV)\right| = \left|\tilde{\gamma}_{V0}^L(HV)\right| = \mathrm{sinc}\left(\frac{\kappa_z^L h_V}{2}\right). \qquad (13)$$

Having an estimate of the (absolute) volume decorrelation contribution at HV permits now to estimate the temporal decorrelation contribution at L- or P- band

$$\gamma_{\mathrm{Temp}} = \left|\tilde{\gamma}(HV)\right| / \left|\tilde{\gamma}_{V0}^L(HV)\right|. \qquad (14)$$

Equation (14) has been finally used to estimate the temporal decorrelation in two L-band and one P-band wind-affected repeat-pass interferograms. The temporal baseline for all three interferograms is on the order of 40 min. A relative homogeneous area of about 1000×1000 m has been selected in order to reduce the impact of forest inhomogeneity. An X-band amplitude image of the selected area is shown in the top figure of Fig. 16, demonstrating the homogeneity of the forest. The estimated γ_{Temp} maps are shown below in Fig. 16. The decorrelation patterns do not correlate with the forest structure and change from interferogram to interferogram; the wisplike decorrelation patterns are typical for wind-induced decorrelation. The corresponding histograms are shown in Fig. 17. At L-band, γ_{Temp} is about 0.89 for the first interferogram and 0.85 for the second, while at P-band, γ_{Temp} is, as expected, higher and about 0.93.

Note that a potential underestimation of the forest height by using (14) (caused, for example, by saturation) will bias the volume decorrelation estimation and lead to an underestimation of the temporal decorrelation. On the contrary, an overestimation of the forest height (due to an underestimated extinction) will lead to an overestimation of the temporal decorrelation or even to ratios larger than one. The localized high decorrelation "points" visible at L-band and even more at P-band are due to single large trees that are underestimated when inverting the X-band coherence, leading therefore to high temporal decorrelation regions.
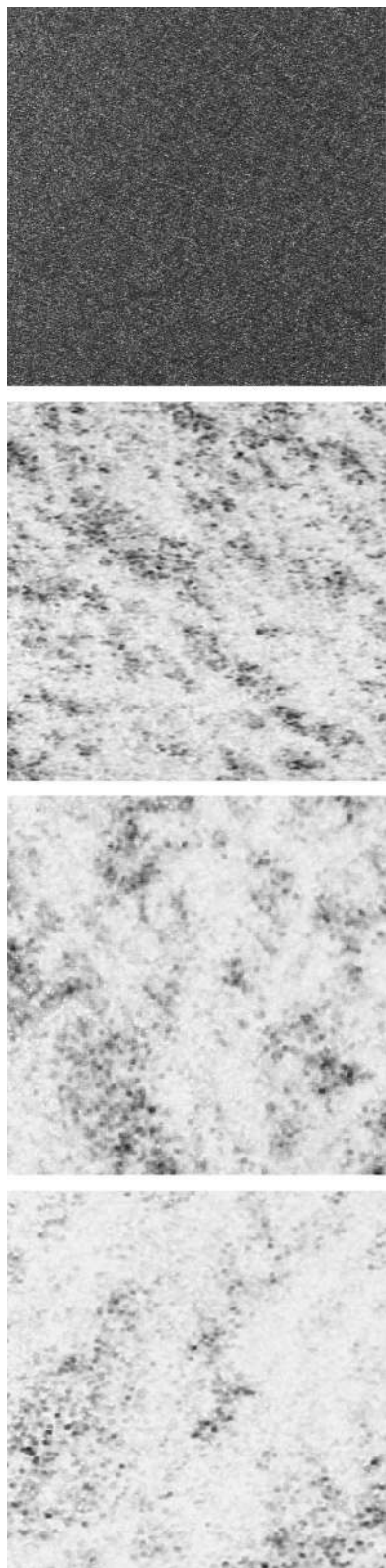
Fig. 16. (Top; grayscale) Amplitude and (middle two) estimated temporal decorrelation images at L- and (bottom) P-band for the Mawas Dome test site scaled from black: $\gamma_{\text{Temp}} = 0$ to white: $\gamma_{\text{Temp}} = 1$. 1000×1000 m.

Fig. 17. Histograms of estimated temporal decorrealtion, (Solid and dashed lines with a mean of 0.89 and 0.85 respectively) at L-band and (dotted line with a mean of 0.93) at P-band for temporal baselines on the order of 40 min at Mawas Dome test site.

VII. DISCUSSION AND CONCLUSION

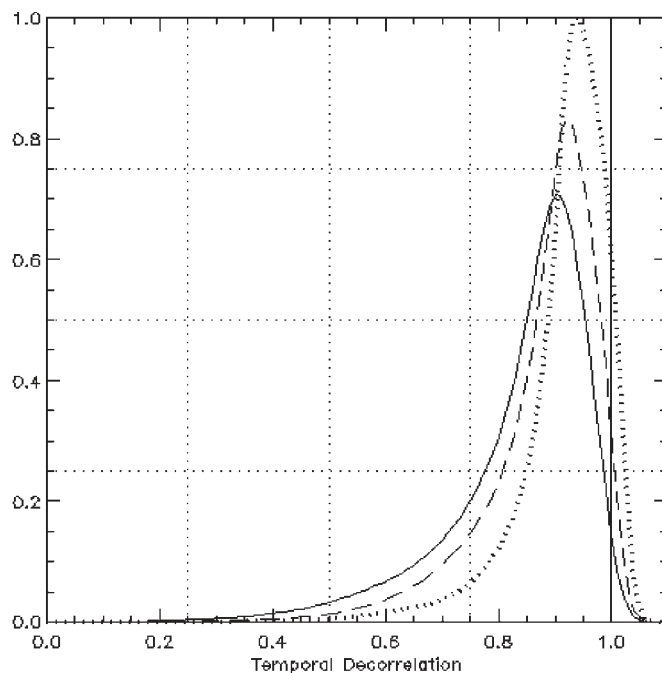In this paper, the analysis, inversion, and validation of Pol-InSAR data collected in the frame of the INDREX-II campaign have been addressed and discussed. From the six INDREX-II test sites, the two most important in terms of available ground measurements and forest conditions have been selected for the investigations presented. The selected test sites include typical (disturbed and undisturbed) forest formations of Southeast Asia like dense lowland dipterocarp and peat-swamp forests which are the most important regional forest types.

First, the question about the visibility of the ground was faced. The polarimetric and interferometric analysis of the Sungai Wain data in Section IV demonstrated clearly the capability of both frequencies, L- and P-band, to penetrate until the ground through dense dipterocarp forests, with individual tree heights up to 60 m and local biomass levels even beyond 600 t/ha. This is a significant result toward the implementation of a low-frequency spaceborne SAR observation system.

The forest-height inversion performance has been assessed in Section V. In the case of the Sungai Wain test site, the Pol-InSAR estimates have been validated against H100 values estimated from the ground measurements. For forest heights ranging from 15 up to 45 m, the L- and P-band estimates where within 10% accuracy, even in hilly terrain. For the Mawas River test site, the validation was done against the LIDAR-derived H100. For forest heights ranging from 5 to 27 m, L-band estimates where characterized by an r^2 of 0.91 with an RMSE of 1.97 m, while the best P-band estimates show an r^2 of 0.94 with an RMSE of 1.74 m. The overall estimation accuracy for both test sites was better than 10% for both frequencies. The key limiting factor in estimation accuracy appears to be the uncompensated nonvolumetric decorrelation effects, particularly temporal decorrelation.

A key element in the quantitative assessment of temporal decorrelation was the single-pass single-channel (VV) X-band

data set. In a first step, a modification of the conventional Pol-InSAR forest-height inversion scheme has been proposed, adapted to the single-channel X-band interferometric observation space. The neglect of the ground-scattering component and the use of an external (LIDAR-derived) ground DEM allowed us to obtain sensitive height estimates and to validate them against the LIDAR measurements for the Mawas River test site. In the less-dense peat-swamp forest, X-band is able to penetrate until the ground, providing estimates characterized by surprisingly high r^2 values on the order of 0.94 with an RMSE of 1.77 m. This is a strong indication for the potential Pol-InSAR performance expected in the absence of temporal decorrelation. The generalization of the X-band performance is however critical as the visibility of the ground required for unbiased inversion gets lost when going to denser forest conditions. Nevertheless, keeping in mind the high-resolution single-pass X-band Pol-InSAR spaceborne configuration of TanDEM-X [37] scheduled for launch in 2009, the results become significant, particularly with respect to the wall-to-wall mapping of less-dense forest ecosystems as the boreal ones.

In a second step, in Section VI, the X-band height estimates have been used to assess the amount of temporal decorrelation at L- and P-band. Looking at temporal baselines of about 40 min, the obtained results indicate, as expected, a higher temporal stability at P-band (with temporal decorrelation on the order of 0.93) than at L-band (with temporal decorrelation on the order of 0.85–0.89). However, the decorrelation levels are, at both frequencies, sufficient to cause—if not compensated—an overestimation on the order of 30%–40% depending on the actual forest-height level.

In closing, it is important to make clear that the results achieved up to now and the conclusions drawn from the evaluation of this unique data, set point out the scientific importance of challenging and successful campaigns such as INDREX-II.

REFERENCES

[1] A. Rosenqvist, M. Shimada, B. Chapman, A. Freeman, G. de Grandi, S. Saatchi, and Y. Rauste, "The global rain forest mapping project—A review," *Int. J. Remote Sens.*, vol. 21, no. 6/7, pp. 1375–1387, 2000.

[2] A. Rosenqvist, T. Ogawa, M. Shimada, and T. Igarashi, "Initiating the ALOS Kyoto & carbon initiative," in *Proc. IEEE IGARSS*, Toulouse, France, July 2003, pp. 21.–25.

[3] M. J. Quinones and D. Hoekman, "Exploration of factors limiting biomass estimation by polarimetric radar in tropical forests," *IEEE Trans. Geosci. Remote Sens.*, vol. 42, no. 1, pp. 86–104, Jan. 2004.

[4] D. Hoekman and M. J. Quinones, "Biophysical forest type characterization in the Colombian Amazon by airborne polarimetric SAR," *IEEE Trans. Geosci. Remote Sens.*, vol. 40, no. 6, pp. 1288–1300, Jun. 2002.

[5] J. C. Mura, L. Sant'Anna Bins, F. F. Gama, C. Da Costa Freitas, J. R. dos Santos, and L. V. Dutra, "Identification of the tropical forest in Brasilian Amazon based on the DEM difference from P- and X-band interferometric data," in *Proc. IEEE IGARSS*, Sydney, Australia, Jul. 9–13, 2001, vol. 2, pp. 789–791.

[6] T. Neef, G. S. Biging, L. V. Dutra, C. C. Freitas, and J. R. dos Santos, "Markov point processes for modeling of spatial forest patterns in Amazonia derived from interferometric height," *Remote Sens. Environ.*, vol. 97, no. 4, pp. 484–494, Sep. 2005.

[7] T. Neef, L. V. Dutra, J. R. dos Santos, C. C. Freitas, and L. V. Dutra, "Tropical forest measurement by interferometric height modeling and P-band radar backscatter," *For. Sci.*, vol. 51, no. 6, pp. 585–594, Dec. 2005.

[8] D. H. Hoekman and C. Varekamp, "Observation of tropical rain forest trees by airborne high-resolution interferometric radar," *IEEE Trans. Geosci. Remote Sens.*, vol. 39, no. 3, pp. 584–594, Mar. 2001.

[9] C. Varekamp and D. Hoekman, "High-resolution InSAR image simulation for forest canopies," *IEEE Trans. Geosci. Remote Sens.*, vol. 40, no. 7, pp. 1648–1655, Jul. 2002.

[10] S. R. Cloude and K. P. Papathanassiou, "Polarimetric SAR interferometry," *IEEE Trans. Geosci. Remote Sens.*, vol. 36, no. 5, pp. 1551–1565, Sep. 1998.

[11] K. P. Papathanassiou and S. R. Cloude, "Single-baseline polarimetric SAR interferometry," *IEEE Trans. Geosci. Remote Sens.*, vol. 39, no. 11, pp. 2352–2363, Nov. 2001.

[12] J. Praks, F. Kugler, K. P. Papathanassiou, I. Hajnsek, and M. Hallikainen, "Height estimation of boreal forest: Interferometric model-based inversion at L- and X-band versus HUTSCAT profiling scatterometer," *IEEE Geosci. Remote Sens. Lett.*, vol. 4, no. 3, pp. 466–470, Jul. 2007.

[13] F. Kugler, F. N. Koudogbo, K. P. Papathanassiou, and K. Gutjahr, "Frequency effects in POL-InSAR forest height estimation," in *Proc. EUSAR*, Dresden, Germany, May 16–18, 2006.

[14] T. Mette, K. P. Papathanassiou, and I. Hajnsek, "Estimating forest biomass from polarimetric interferometric SAR data in combination with forest allometry—Results from temperate spruce forest test site traunstein," in *Proc. Retrieval Bio Geophys. Parameters SAR Data Land Appl.*, Innsbruck, Austria, Nov. 16–19, 2004.

[15] F. Garestier, P. C. Dubois-Fernandez, and K. P. Papathanassiou, "Pine forest height inversion using single-pass X-band PolInSAR data," *IEEE Trans. Geosci. Remote Sens.*, vol. 46, no. 1, pp. 59–68, Jan. 2008.

[16] S. Magnussen, P. Eggermont, and V. N. La Ricca, "Recovering tree heights from airborne laser scanner data," *For. Sci.*, vol. 45, no. 3, pp. 402–422, Aug. 1999.

[17] J. Hyyppä, H. Hyyppä, M. Inkinen, and M. Engdahl, "Verification of the potential of various remote sensing datasources for forest inventory," in *Proc. IEEE Int. Geosci. Remote Sens. Soc.*, Pasadena, CA, 1998, pp. 1812–1814.

[18] G. Krieger, K. P. Papathanassiou, and S. R. Cloude, "Spaceborne polarimetric SAR interferometry: Performance analysis and mission concepts," *EURASIP J. Appl. Signal Process.*, vol. 2005, no. 1, pp. 3272–3292, Jan. 2005.

[19] R. Bamler and P. Hartl, "Synthetic aperture radar interferometry," *Inverse Probl.*, vol. 14, no. 4, pp. R1–R54, Aug. 1998.

[20] I. Hajnsek, K. P. Papthanssiou, and S. R. Cloude, "Removal of additive noise in polarimetric eigenvalue processing," in *Proc. IEEE IGARSS*, Sydney, Australia, 2001, pp. 2778–2780.

[21] H. A. Zebker and J. Villasenor, "Decorrelation in interferometric radar echoes," *IEEE Trans. Geosci. Remote Sens.*, vol. 30, no. 9, pp. 950–959, Jan. 1992.

[22] R. N. Treuhaft, S. N. Madsen, M. Moghaddam, and J. J. van Zyl, "Vegetation characteristics and underlying topography from interferometric radar," *Radio Sci.*, vol. 31, no. 6, pp. 1449–1495, 1996.

[23] S. R. Cloude and K. P. Papathanassiou, "Three-stage inversion process for polarimetric SAR interferometry," *Proc. Inst. Elect. Eng.—Radar Sonar Navig.*, vol. 150, no. 3, pp. 125–134, Jun. 2003.

[24] F. Kugler, K. P. Papathanassiou, S. K. Lee, I. Hajnsek, H. Pretzsch, "Forest height estimation by means of airborne repeat-pass polarimetric SAR interferometry," to be published.

[25] S. R. Cloude and E. Pottier, "A review of target decomposition theorems in radar polarimetry," *IEEE Trans. Geosci. Remote Sens.*, vol. 34, no. 2, pp. 498–518, Mar. 1996.

[26] Izzawati, E. D. Wallington, and I. H. Woodhouse, "Forest height retrieval from commercial X-band SAR products," *IEEE Trans. Geosci. Remote Sens.*, vol. 44, no. 4, pp. 863–870, Apr. 2006.

[27] H. Balzter, C. Rowland, R. Milne, O. Stebler, G. Patenaude, T. Dawson, and P. Sachi, "Potential of polarimetric SAR interferometry for forest carbon accounting," in *Proc. IEEE IGARSS*, Toulouse, France, 2003, pp. 1945–1947.

[28] M. Tabb, J. Orrey, T. Flynn, and R. Carande, "Phase diversity: A decomposition for vegetation parameter estimation using polarimetric SAR interferometry," in *Proc. EUSAR*, 2002, pp. 721–724.

[29] T. Flynn, M. Tabb, and R. Carande, "Coherence region shape extraction for vegetation parameter estimation in polarimetric SAR interferometry," in *Proc. IEEE IGARSS*, Toronto, ON, Canada, Jun. 2002, vol. 5, pp. 2596–2598.

[30] E. Colin, C. Tintin-Schnaider, and W. Tabbarra, "An interferometric coherence optimization method in radar polarimetry for high-resolution imagery," *IEEE Trans. Geosci. Remote Sens.*, vol. 44, no. 1, pp. 167–175, Jan. 2006.

[31] R. T. Fomena and S. R. Cloude, "On the role of coherence optimization in polarimetric SAR interferometry," in *Proc. CEOS SAR CAL/VAL Workshop*, Adelaide, Australia, Sep. 28–30, 2005.

[32] T. Mette, K. P. Papathanassiou, and I. Hajnsek, "Biomass estimation from polarimetric SAR interferometry over heterogeneous forest terrain," in *Proc. IEEE IGARSS*, Anchorage, AK, Sep. 20–24, 2004, pp. 511–514.

[33] H. Kramer and A. Akca, *Leitfaden zur Waldmesslehre*. Frankfurt, Germany: Sauerländer, 1995, p. 145.

[34] T. Aulinger, T. Mette, K. P. Papathanssiou, I. Hajnsek, M. Heurich, and P. Krzystek, "Validation of heights from interferometric SAR and LIDAR over the temperate forest site 'national park bayerischer wald'," in *Proc. 2nd Int. Workshop POLinSAR*, Frascati, Italy, Jan. 17–21, 2005. CD.

[35] R. Horn, "The DLR airborne SAR project E-SAR," in *Proc. IEEE Geosci. Remote Sens. Symp.*, Lincoln, NE, May 1996, vol. 3, pp. 1624–1628.

[36] K. P. Papathanassiou and S. R. Cloude, "The effect of temporal decorrelation on the inversion of forest parameters from Pol-InSAR data," in *Proc. IEEE IGARSS*, Toulouse, France, 2003, pp. 1429–1431. CD-ROM.

[37] G. Krieger, A. Moreira, H. Fiedler, I. Hajnsek, M. Werner, M. Younis, and M. Zink, "TanDEM-X: A satellite formation for high-resolution SAR interferometry," *IEEE Trans. Geosci. Remote Sens.*, vol. 45, no. 11, pp. 3317–3341, Nov. 2007.

Florian Kugler was born in Bavaria, Germany, in 1974. He received the Dipl. Ing. Silv. degree in forestry science from the Technische Universität München, Freising, Germany, in 2004. He is currently working toward the Ph.D. degree in the Microwaves and Radar Institute, German Aerospace Center, Wessling, Germany.

His research interests include remote sensing on forests using polarimetric synthetic aperture radar interferometry.

Seung-Kuk Lee received the B.S. and M.S. degrees in earth system sciences from Yonsei University, Seoul, Korea, in 2000 and 2005, respectively. He is currently working toward the Ph.D. degree in the Microwaves and Radar Institute, German Aerospace Center (DLR), Wessling, Germany.

Since 2007, he has been with Microwaves and Radar Institute, DLR, as a Guest Scientist, through a scholarship from the Korea Research Foundation. His research interests include polarimetric synthetic aperture radar interferometry.

Irena Hajnsek (A'01–M'01) received the Dipl. degree (with honors) from the Free University of Berlin, Berlin, Germany, in 1996 and the Ph.D. degree (with honors) from the Friedrich Schiller University of Jena, Jena, Germany, in 2001.

From 1996 to 1999, she was a Project Scientist with the Microwaves and Radar Institute, German Aerospace Center (DLR), Wessling, Germany. From 1999 to 2000, she was an European Union Fellow with the Institut d'Electronique et de Telecommunications de Rennes, University of Rennes I, Rennes, France, for ten months, and with Applied Electromagnetics, St. Andrews, U.K., for four months. In 2000, she rejoined the Radar Concepts Department, Microwaves and Radar Institute, DLR, where she has been leading the Polarimetric SAR Interferometry Research Group since 2002. In 2005, she was a Visiting Scientist at The University of Adelaide, Adelaide, Australia. She is responsible for the polarimetric science exploration of TerraSAR-X and is the Coordinator of the TanDEM-X science team. Her current research interests include electromagnetic propagation and scattering theory, radar polarimetry, synthetic aperture radar (SAR) and interferometric SAR data processing techniques, and environmental parameter modeling and estimation.

Dr. Hajnsek is the recipient of the DLR Science Award in 2002.

Konstantinos Panagiotis Papathanassiou (M'02–SM'03) received the Dipl.Ing. degree (with honors) and the Ph.D. degree (with honors) from the Technical University of Graz, Graz, Austria, in 1994 and 1999, respectively.

From 1992 to 1994, he was with the Institute for Digital Image Processing, Joanneum Research, Graz. From 1995 to 1999, he was with the Microwaves and Radar Institute, German Aerospace Center (DLR), Wessling, Germany. From 1999 to 2000, he was a European Union Postdoctoral Fellow with Applied Electromagnetics, St. Andrews, U.K. In October 2000, he rejoined the Radar Concepts Department, Microwaves and Radar Institute, DLR, where he is currently a Senior Scientist within the Polarimetric SAR Interferometry (Pol-InSAR) Research Group, working on Pol-InSAR and the development of inversion algorithms for physical parameters from synthetic aperture radar (SAR) data. He is the author of more than 100 publications in international journals and conference and workshop proceedings. His research interests include polarimetric and interferometric processing and calibration techniques, polarimetric SAR interferometry, quantitative parameter estimation from SAR data, and SAR mission design and performance analysis.

Dr. Papathanassiou was the recipient of the IEEE Geoscience and Remote Sensing Society International Geoscience and Remote Sensing Symposium Prize Paper Award in 1998, the Best Paper Award of the European SAR Conference in 2001, and the DLR Science Award in 2002.